Journal of Quantitative Spectroscopy & Radiative Transfer ■ (■■■■) ■■■–■■■

Contents lists available at ScienceDirect

Journal of Quantitative Spectroscopy & Radiative Transfer

journal homepage: www.elsevier.com/locate/jqsrt

Neural network radiative transfer solvers for the generation of high resolution solar irradiance spectra parameterized by cloud and aerosol parameters

M. Taylor [a,*], P.G. Kosmopoulos [a], S. Kazadzis [a,b], I. Keramitsoglou [c], C.T. Kiranoudis [c,d]

[a] Institute for Environmental Research and Sustainable Development (IERSD), National Observatory of Athens (NOA), Metaxa & Vas Pavlou, Penteli, GR-15236 Athens, Greece

[b] Physikalisch-Meteorologisches Observatorium Davos, World Radiation Center (PMOD/WRC), Dorfstrasse 33, CH-7260 Davos Dorf, Switzerland

[c] Institute for Astronomy, Astrophysics, Space Applications & Remote Sensing (IAASARS), National Observatory of Athens (NOA), Metaxa & Vas Pavlou, Penteli, GR-15236 Athens, Greece

[d] School of Chemical Engineering, National Technical University of Athens (NTUA), GR-15780 Athens, Greece

ARTICLE INFO

Article history:
Received 30 June 2015
Accepted 28 August 2015

Keywords:
Solar radiation
Clouds
Aerosol
Neural networks
Radiative transfer

ABSTRACT

This paper reports on the development of a neural network (NN) model for instantaneous and accurate estimation of solar radiation spectra and budgets geared toward satellite cloud data using a ≈2.4 M record, high-spectral resolution look up table (LUT) generated with the radiative transfer model libRadtran. Two NN solvers, one for clear sky conditions dominated by aerosol and one for cloudy skies, were trained on a normally-distributed and multiparametric subset of the LUT that spans a very broad class of atmospheric and meteorological conditions as inputs with corresponding high resolution solar irradiance target spectra as outputs. The NN solvers were tested by feeding them with a large (10 K record) "off-grid" random subset of the LUT spanning the training data space, and then comparing simulated outputs with target values provided by the LUT. The NN solvers demonstrated a capability to interpolate accurately over the entire multiparametric space. Once trained, the NN solvers allow for high-speed estimation of solar radiation spectra with high spectral resolution (1 nm) and for a quantification of the effect of aerosol and cloud optical parameters on the solar radiation budget without the need for a massive database. The cloudy sky NN solver was applied to high spatial resolution (54 K pixel) cloud data extracted from the Spinning Enhanced Visible and Infrared Imager (SEVIRI) onboard the geostationary Meteosat Second Generation 3 (MSG3) satellite and demonstrated that coherent maps of spectrally-integrated global horizontal irradiance at this resolution can be produced on the order of 1 min.

1. Introduction

The 5th assessment report of the International Panel on Climate Change [21] has highlighted a need for increasing the breadth of studies into the impact of clouds, aerosols and their feedback processes on climate change. The main reason for this emphasis is that there is uncertainty in the sensitivity of the Earth climate system to the global

* Corresponding author. Tel.: +30 2108109170; fax: +30 2108103236.
E-mail address: mtaylor@noa.gr (M. Taylor).

http://dx.doi.org/10.1016/j.jqsrt.2015.08.018
0022-4073/

radiation balance [52]. Questions are also being raised about the reliability of assessments of the level of uncertainty associated with direct aerosol radiative forcing [23]. Importantly, clouds are known to affect the energy balance of the Earth system by influencing both shortwave solar radiation and longwave terrestrial radiation [1,37]. The radiative properties of clouds depend on their height, the size of constituent water or ice droplets and optical properties. An increase of cloud top height reduces outgoing infrared radiation and leads to an increase in tropospheric and surface temperature, which in turn can affect the radiative interaction of clouds with solar and terrestrial radiation [5]. For example, the introduction of solar UV flux into a spectral GCM coupled to a chemical transport model was shown to lead to an intensification of the polar vortex and a statistically significant surface warming of up to 1.2 K over North America and Siberia [11]. Importantly, cloud optical properties have been found to have a direct influence on climate via various feedback mechanisms [3]. While changes in cloud water content are known to have a strong impact on different environmental scenarios, large uncertainty has been found to be associated with cloud optical properties and cloud-climate feedback mechanisms in particular. Moreover, because clouds and aerosols are closely related in the climate system [26,3], the influences of internal/external mixing of aerosol need to be considered since they may significantly alter cloud optical properties and their influence on the radiation budget [28].

The magnitude of the uncertainty due to the effect of clouds on large-scale radiation budgets is much less well constrained than that due to aerosol and has motivated a number of studies. As part of the International Satellite Cloud Climatology Project (ISCCP), Zhang et al. [60] estimated top of the atmosphere and surface radiative fluxes using a radiative transfer model, and used the derived radiation budget to analyze the distribution of cross-zonal heating and cooling; an important input in climate models. Surface radiation budgets have also been estimated in the context of global surface temperature by capitalizing on the full-Earth viewing potential offered by geostationary satellite observations in conjunction with general circulation models (GCM) and/or online coupled numerical weather prediction models [42,43,59], and have been shown to be sensitive to cloud feedback processes [53,56]. This has also been confirmed by radiative-convective models which have demonstrated the sensitivity of climate to cloud optical properties and the related feedback processes [19].

Findings such as these highlight the need for more detailed studies of the influence of clouds and aerosol and their feedback processes on the Earth system and on radiation budgets. To achieve this, new and efficient parameterizations in terms of cloud and aerosol are required to reduce the uncertainty associated with radiative forcing. An important step in this direction was the work of Takenaka et al. [54] who developed a customized neural network (NN) solver based on radiative transfer calculations from the radiative transfer code RSTAR5b [35,36] to estimate downward and upward shortwave fluxes at the surface and the top of the atmosphere from combined aerosol and cloud parameters with high speed and accuracy. It should be borne in mind that there is a growing number of radiative transfer codes which vary substantially in the numerical approximation method used (e.g. discrete ordinates and/or 2-stream), their spectral resolution (UV, visible, near-IR, thermal-IR, mm/sub-mm and microwave), their treatment of cloud properties and gas absorption (principal and/or trace), the complexity of their aerosol models, whether or not they perform line-by-line (LBL) flux or band integration, their inclusion of scattering and polarization, the geometry adopted as well as atmospheric profiles and surface characteristics. The Intercomparison of Radiation Codes in Climate Models (ICRCCM; http://gcmd.nasa.gov/records/GCMD_CDIAC_ICRCCM.html) under the auspices of the World Meteorological Organization (WMO) produced benchmark longwave LBL fluxes to allow for their assessment [12]. However, researchers have had to deal with the trade off between calculation speed and accuracy. On the one hand, the estimation of radiances for finite spectral intervals (e.g. to estimate solar energy budgets) with LBL calculations is precise but computationally intensive, while on the other hand, band-integrated irradiances are faster but imprecise. The Continual Intercomparison of Radiation Codes (CIRC; http://circ.gsfc.nasa.gov/) has emphasized the importance of using observations to constrain and define intercomparison cases [40] and more recently, emphasis has been placed on computational speed with new parameterizations of bands and channels to accelerate radiance calculations and to provide a good compromise between computation time and uncertainty for a range of typical radiative transfer problems, in particular, for satellite radiometer simulations [15]. Current trends suggest that the greatest gains in speed are expected to come from NN models or hybrid approaches that incorporate NNs.

Building on the work of Lopez et al. [30], Dorvlo et al. [10], Zarzalejo et al. [58] and Takenaka et al. [54] which pioneered the development of NN models of solar radiation, here we report on the development of NN solvers for radiance spectra parameterized in terms of cloud and aerosol:

i. that are based on large state-of-the-art LUTs calculated with libRadtran that span a very broad range of cloud and atmospheric conditions,
ii. that include cloud optical parameters which are derived from a new tailor-made satellite product for the development of radiation budget applications,
iii. that recover the UV, visible and near-IR radiation spectra at high resolution (1 nm),
iv. and which, once trained, can produce almost instantaneous output.

To train and validate the NN, we constructed two high resolution LUTs from a total of ≈ 2.5 million runs with the radiative transfer code, libRadtran [32] for clear sky and cloudy conditions (separately) using distributed computing over a network of 8 high-end workstations running continuously in batch mode for ≈ 3 months. The trained NNs developed here behave like fast radiative transfer solvers and have been designed to meet the need for both

Please cite this article as: Taylor M, et al. Neural network radiative transfer solvers for the generation of high resolution solar irradiance spectra parameterized by cloud and aerosol parameters. J Quant Spectrosc Radiat Transfer (2015), http://dx.doi.org/10.1016/j.jqsrt.2015.08.018

speed and high accuracy in multivariate studies of cloud–radiation–aerosol interactions in the atmosphere, as well as for production of real-time maps of solar irradiance from real-time satellite inputs.

The rest of this report is arranged as follows. Section 2 presents the data used to train and validate two NN solvers; in particular, the construction of large and high resolution radiative transfer LUTs for clear sky and cloudy conditions. Section 3 describes the general NN model and provides details of the training and validation process. Section 4 presents the results of testing the NN solvers on a large and representative sample of parameter values as well as their application to the production of high spatial resolution solar irradiance maps using satellite cloud data inputs. We conclude in Section 5 with a summary of the key findings and with a discussion of potential applications of this approach.

2. Data

2.1. Solar irradiance LUTs for clear and cloudy sky conditions

In order to construct reliable and comprehensive radiative transfer LUTs for clear and cloudy sky conditions, it was necessary in each case, to compile a list of the minimal set of input parameters required for calculation of solar irradiance spectra: the global horizontal irradiance (GHI), direct normal irradiance (DNI), diffuse horizontal irradiance (DHI) and the actinic flux (AF), at the surface. For both clear and cloudy sky conditions, the solar zenith angle (SZA) and total ozone in the atmospheric column (TOC) are key input parameters. SZA is a geometrical parameter of solar irradiance calculated from the Brewer angle and is dependent on the relative positions of the Sun, Moon and Earth at each point on the surface (specified by latitude and longitude), while TOC is the most important principal gas known to absorb short-wave (SW) radiation. When modeling clouds, the cloud optical thickness (COT), from which we distinguish between the water cloud optical thickness (WCOT) and ice cloud optical thickness (ICOT), is key parameters associated with cloud water or ice droplet scattering. In our calculations, droplets were assumed to be spheres having typical climatological mean heights and values of effective radius (R_{eff}). In particular, for low-lying water clouds, we used the value $R_{\mathrm{eff}}=10\ \mu$m and three values of the liquid water path (LWP): 1 g/m^3 at 2 km, 2 g/m^3 at 3 km and 0 g/m^3 at 4 km. For ice clouds at 10 km we used: $R_{\mathrm{eff}}=20\ \mu$m and LWP$=0.005$ g/m^3, and for ice clouds at 11 km: $R_{\mathrm{eff}}=0\ \mu$m and LWP$=0$ g/m^3. Hess et al. [17] provide a detailed overview of the optical properties of aerosols and clouds at different altitudes. All optical thicknesses (water, ice and also aerosol) in our runs are calculated at 550 nm. When modeling clear sky radiance, aerosol has a particularly important impact on the radiation budget [52] and hence the aerosol optical thickness (AOT), the Angstrom Exponent (AE), and the single scattering albedo (SSA) are included in our clear sky aerosol model. In particular, the AE is considered to be a good proxy of particle size and hence to have an impact on scattering while the SSA is considered to be a good proxy for absorption. Furthermore, the total columnar water vapor (which we will denote "H_2O") is an additional principal gas known to strongly absorb short-wave ("SW") radiation, and is included. Regarding the choice of aerosol parameters, the 6-input clear sky parameters were chosen so as to cover: (a) a wide range of precipitable water loadings, (b) a significant range of aerosol loadings and types (as expressed through the combination of AOT, AE and SSA) and (c) a significant range of solar angles – as these have been found to be important factor on the performance of radiative transfer models of the surface solar radiation [20,39]. Regarding the cloud parameters, the principal aim of our model is to develop a model that can be driven by MSG–SEVIRI cloud products and hence the 4 input variables in the cloudy sky NN model were carefully chosen to be aligned with the cloud products provided by MSG. Based on these two sets of minimal aerosol and cloud parameters, input files for the radiative transfer code libRadtran were generated by permuting parameter combinations over a range of step-sizes. Each run of libRadtran then produced GHI, DNI, DHI and AF output spectra. Table 1 presents the parameters applied in the radiative transfer calculations for construction of the clear sky and cloudy sky LUTs, their abbreviation, measurement unit, range of values and step-size used.

The text files comprising the 2 LUTs are quite large and occupy ≈ 2.5 TB. The clear sky LUT comprises 2,100,560 records and the cloudy sky LUT comprises 465,124 records. In total, some 2,565,684 radiative transfer simulations were performed complete with output spectra of the GHI, DNI, DHI and AF. The output wavelength range of the radiative fluxes is 285–1050 nm for the clear sky LUT and 285–2600 nm and for the cloudy sky LUT (so as to incorporate also the effect of H_2O absorption in the near to mid-infrared). All output spectra have a wavelength resolution

Table 1
Input parameters of the radiative transfer LUTs used to train the NN solvers. Note that both LUTs have the same parameter values for the SZA and the TOC.

Input parameter	Abbreviation	Unit	Clear sky LUT	Cloudy sky LUT
Solar zenith angle	SZA	deg	2:2:88	2:2:88
Water cloud optical thickness	WCOT	1		0:1:30
Ice cloud optical thickness	ICOT	1		0:1:30
Total ozone column	TOC	DU	250:20:450	250:20:450
Aerosol optical thickness	AOT	1	0:0.05:1.5	
Angstrom exponent	AE	1	0.2:0.6:2.0	
Single scattering albedo	SSA	1	0.6:0.1:1.0	
Columnar water vapor	H2O	cm	0.5:0.5:3.5	

Please cite this article as: Taylor M, et al. Neural network radiative transfer solvers for the generation of high resolution solar irradiance spectra parameterized by cloud and aerosol parameters. J Quant Spectrosc Radiat Transfer (2015), http://dx.doi.org/10.1016/j.jqsrt.2015.08.018

of 1 nm. Regarding the different spectral ranges used for the clear sky and cloudy sky models, we would like to point out that the clear sky NN model was constructed over a shorter wavelength range for 3 reasons. Firstly, to compare outputs with surface measurements from precision solar radiometers (PSR) instruments which operate in this range. The second reason is that, since the clear sky LUT has 6 input parameters (compared to 4 input parameters for the cloudy sky LUT), extending the spectral range to 2600 strongly impacts on the modeling process by meaning that the construction of the LUT would have taken much longer than the already heavy computational time investment (≈ 3 months continuous runs on 5 multicore PCs). We wish to emphasize that for solar energy applications, the cloudy sky NN with its larger wavelength coverage (285–2600 nm) is the priority due to the effect of COT on the magnitude of the level of the surface solar radiation. Thirdly, the clear sky model was also designed to facilitate an investigation into the dependence of the irradiance spectrum on particular aerosol parameters.

While line-by-line calculation is the most precise way to calculate the spectra, it is far too slow for the construction of LUTs on the scale constructed here. Instead, we adopted a band parameterization based on the correlated-*k* approximation [13,24,61] and the exponential sum fitting technique. This method has been found to be able to offer accurate estimates of the spectral irradiance in spectral intervals comparable with those provided by detailed line-by-line calculations in clear sky and cloudy conditions [38] and is a compromise between speed and accuracy. In the libRadtran run we used the default aerosol model according to Shettle [50]. Regarding the specification of the extraterrestrial solar source spectrum, solar flux data was taken from Kurucz [27] for the cloudy sky runs and from the code for spectral irradiance (COSI) developed in 1D [16,49] for the clear sky runs. Note that the two radiative source setups are different for the clear sky and cloud sky models. The reason for this is that the Kurucz [27] configuration is valid up to 10,000 nm while the COSI configuration [16,49] has higher spectral resolution but is only valid up to 1050 nm which is the upper operating limit of PSR instruments. Since, as mentioned above, planned applications for the clear sky and cloud sky models are clearly separated, this does not cause a conflict. We would like to emphasize also here that, while an estimate of the clear sky spectrum can be obtained with the cloudy sky NN by setting cloud COT values to zero, direct comparison with the clear sky model is not possible because this would require specification of the AOD and H_2O aerosol parameters in the cloudy sky NN model. In a future work we will construct a NN model for investigation of mixed aerosol/cloud conditions. To model gas absorption, the parameterization of molecular bands provided by LOWTRAN [25,45] were used together with 32 standard gas type based on the U.S. Standard Atmosphere [33] and the atmospheric pressure and surface albedo were set to constant values of 1000 hPa and 0.03 respectively so as to exclude the effects of complex topography. The radiative transfer equation is then numerically integrated with a discrete ordinate radiative transfer solver [51] that has a numerically stable algorithm for solving the equations of plane-parallel radiative transfer in a vertically in homogeneous atmosphere [46]. The radiative transfer solver we used is called SDISORT and is the "pseudospherical" analog of the DISORT solver described in Stamnes et al. [51] and which caters for large (twilight) angles ($SZA > 80^\circ$) as described by Dahlback and Stamnes [7]. This choice of solver ensures that the spectra output from our libRadtran simulations are valid from 0° to 90°.

2.2. Cloud data from satellite

In addition to the LUTs used to train and test the 2 NN models which will be described in Section 3 (and validated in Section 4), we obtained satellite cloud data products in order to assess the speed and accuracy of the coudy sky NN model for producing near-real time solar irradiance maps. To accomplish this, the Spinning Enhanced Visible and Infrared Imager (SEVIRI) onboard; the Meteosat Second Generation 3 (MSG3) satellite was utilized to provide the cloud type (CT), cloud phase (CP) product and a tailor-made product for the cloud optical thickness (COT). Cloud phase allows for recognition of whether or not a simulated cloud pixel presents ice or water radiative transfer characteristics, cloud type allows for identification of their height and effective radius, while COT allows for a quantification of the attenuation of incoming solar radiation. The geostationary orbit of MSG3 at 36,000 km above the Earth, allows for continuous monitoring of the Earth disk every 15 min, however with a coarse spatial resolution of approximately $0.05^\circ \times 0.05^\circ$. Following raw MSG-SEVIRI data acquisition by the station, pre-processing of data is performed. The result is a radiance image of the Earth disk depicting Europe, Africa and South America (partly). Subsequently, clouds are identified and their properties are extracted using the Satellite Application Facility for Nowcasting Weather Conditions software (SAFNWC, [34,9]). Note that in the current implementation, Numerical Weather Predictions (NWP) are retrieved from the Global Forecasting System (GSF of the U.S. National Climatic Data Center) for the entire Earth with a grid size of 5°. This step is performed utilizing a sophisticated multi-spectral threshold method that employs different criteria for areas located at daytime, nighttime and twilight. The products of interest (i.e. CT, CP and COT) are provided for the entire Earth disk and then appropriate latitude and longitude datasets are used to extract a region of interest (ROI): Greece in the case of this study. CT is a standard output product of the SAFNWC computational procedure, while COT extraction required an appropriate intervention in the process chain to be implemented. A stereoscopic rotation of this initial data was performed (illustrated in Fig. 1) together with resolution adaptation to overcome gaps resulting from the conversion of spheroids.

As a result of this processing, high spatial resolution maps were obtained that had synchronous values of cloud phase, type and COT, together with the SZA. Since satellite and ground-based remote sensing instruments do not yet provide aerosol data (AOT, AE, SSA and H_2O) at this temporal and spatial resolution, only satellite cloud data is used here with the purpose of assessing the feasibility of generating real-time solar irradiances via NN models.

Please cite this article as: Taylor M, et al. Neural network radiative transfer solvers for the generation of high resolution solar irradiance spectra parameterized by cloud and aerosol parameters. J Quant Spectrosc Radiat Transfer (2015), http://dx.doi.org/10.1016/j.jqsrt.2015.08.018

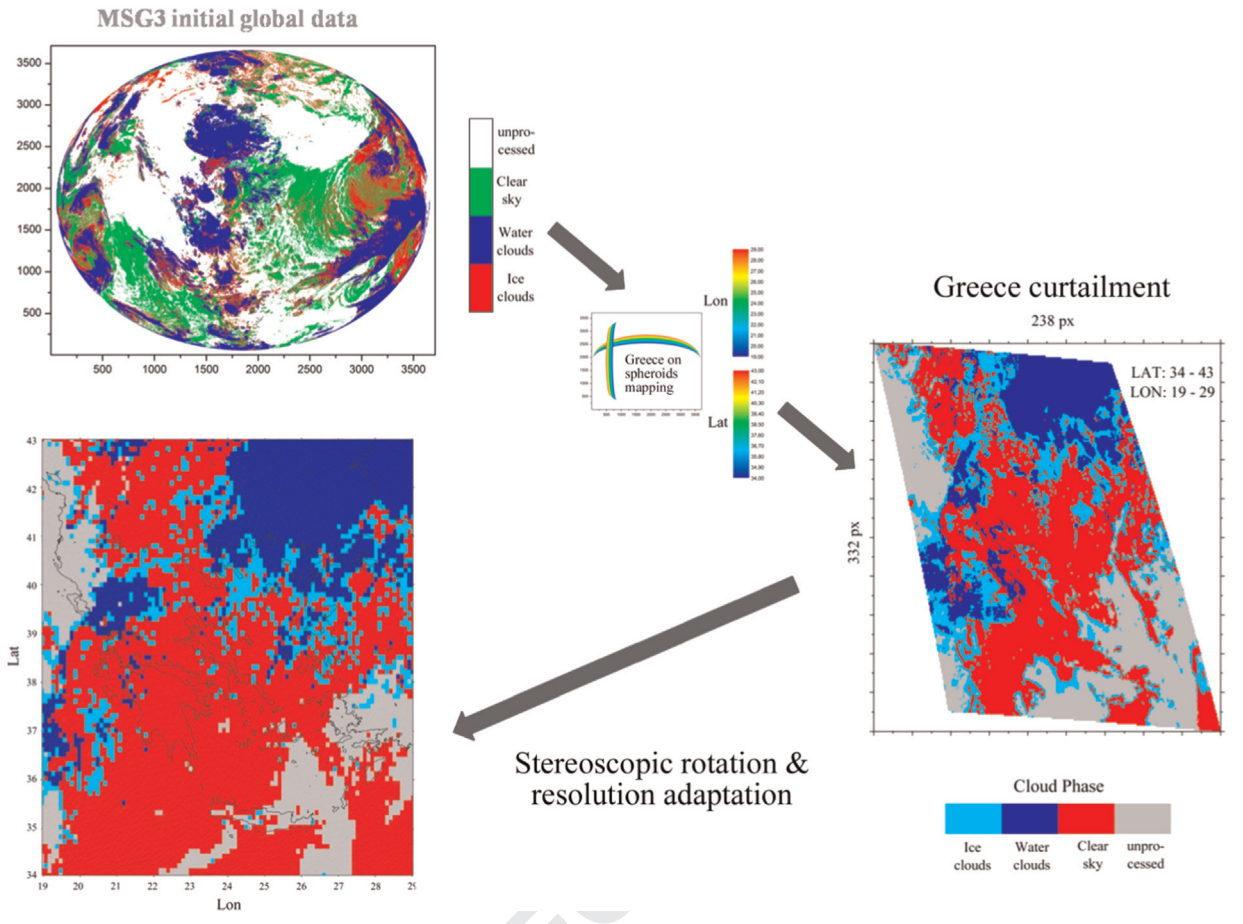

Q3 **Fig. 1.** Processing steps from the initial global MSG3 cloud products to the final stereoscopically-rotated map for the case of the cloud phase product.

3. Methodology

One thing that should be noted is that while satellite cloud data is continuous, cloudy sky LUTs are discrete. For real-world applications based on cloud data, this creates the need for either: i) an interpolating function to be applied to adjacent/nearest-value LUT parameter sets, or ii) a continuous function-approximating model that is valid over the span of values of the LUT. In order to assess the viability of (i), we coded an interpolation algorithm in MATLAB's object-oriented scripting language to solve the following equation: $GHI(\lambda) = f(WCOT, ICOT, SZA, TOC)$ using a grid of 480 input-output vectors much coarser than the LUT: WCOT=0:10:30, ICOT=0:10:30, SZA=0:10:90, and TOC=250:100:450 and corresponding GHI spectra from 285:1:2600 nm. However, this approach was found to be excessively computationally-expensive with each interpolation calculation requiring a time in excess of each single run of libRadtran used to generate the LUT in the first place. Indeed, it has already been noted by researchers in the field that the inclusion of many parameters and small step sizes can dramatically increase the LUT volume [54] and that the multidimensional nature of the dataset requires interpolation/extrapolation procedures that impact strongly on calculation speed [14,48]. As a result, we opted for (ii) and proceeded to construct, train and validate a NN model that is a continuous function-approximator and which, once trained, produces instantaneous output solar irradiance spectra per input vector. This makes NN models suitable for real-time applications where radiation spectra are required at high frequency (e.g. 1 every 15 min). to match the frequency of output from geostationary satellites like MSG3). As will be demonstrated in Section 4.4 in the context of producing high spatial resolution regional maps of spectral radiation estimates (e.g. 54k pixels are needed for Greece and scaling up to regions the size of Europe requires millions of pixels), the capacity of NNs to produce instantaneous spectral output makes them preferable to interpolation-based alternative approaches.

3.1. The NN model

In this section, we describe a generic continuous function-approximating NN model for retrieval of solar irradiance spectra (outputs) from cloud and aerosol parameters (inputs). For multivariate input–output data, a feed-forward NN having at least one layer of "hidden" neurons whose activation functions are nonlinear hyperbolic tangent functions or other general nonlinear sigmoidal functions, has been proven to be a universal function approximator ([6]; Hornik et al. 1989). This means that, given enough hidden neurons and training data, such networks are

Please cite this article as: Taylor M, et al. Neural network radiative transfer solvers for the generation of high resolution solar irradiance spectra parameterized by cloud and aerosol parameters. J Quant Spectrosc Radiat Transfer (2015), http://dx.doi.org/10.1016/j.jqsrt.2015.08.018

capable of learning the mathematical relation between inputs and outputs. The input and output vectors used in our study were connected via 2 network layers – the first containing hidden neurons with *Tanh* activation functions, and the second containing output neurons with linear activation functions as depicted in Fig. 2.

The exact mathematical equation relating the NN outputs to the NN inputs for this type of NN model is given by the matrix equation [55]:

$$\mathbf{Y} = f^2\left(\mathbf{LW}^{2,1} f^1\left(\mathbf{IW}^{1,1}\mathbf{X} + b^1\right) + b^2\right) \quad (1)$$

The multiplication of the matrix $\mathbf{IW}^{1,1}$ and the vector $\mathbf{X}$ is a dot product equivalent to the summation of all input connections to each neuron in the hidden layer. Eq. (1) is the continuous (nonlinear) functional approximation that relates the output vector to the input vector. The NN model was coded using MATLAB's object-oriented scripting language in conjunction with its Neural Network Toolbox [8]. Such NN models require specification of how the performance error associated with the network model is to be measured and also neural network architecture. We measure the performance error of the network via the mean squared error (MSE) calculated from the difference between NN outputs (y_i) and libRadtran target values (t_i). During each iteration of the learning process, the weights and biases are tuned so as to minimize the MSE cost function:

$$\mathrm{MSE} = \frac{1}{N}\sum_{i=1}^{N} |t_i - y_i|^2 \quad (2)$$

over the set of N input–output vectors. In this report, when comparing model outputs with target data, we calculate the root mean squared error (RMSE), the mean absolute error (MAE), the bias (b) and the percentage fractional error (PFE):

$$\mathrm{RMSE} = \sqrt{\frac{1}{N}\sum_{i=1}^{N} |t_i - y_i|^2} \quad (3)$$

$$\mathrm{MAE} = \frac{1}{N}\sum_{i=1}^{N} |t_i - y_i| \quad (4)$$

$$\mathrm{b} = \frac{1}{N}\sum_{i=1}^{N} (t_i - y_i) \quad (5)$$

$$\mathrm{PFE} = \frac{(t_i - y_i)}{t_i} \times 100\% \quad (6)$$

as statistical measures of the average error (or difference) – and which have the same units as the data. The PFE is used in this paper for comparing maps of quantitue. The Pearson product–moment correlation coefficient, R [41] is calculated as a linear regression measure when comparing spectrally-integrated irradiance. When comparing the quality of models to recreate spectral dependence of irradiance with wavelength, the coefficient of determination, R^2 (see for example: [4]) is calculated.

In order to identify the optimal NN architecture for the NN model, we then adopted the approach developed in Taylor et al. [55] where by: all input and output variables are normalized to their z-score values, principal components analysis (PCA) is applied separately to input and output vectors to eliminate parameter redundancy (while retaining 98% of the variance), the number of hidden neurons and the proportion of training data are varied, and the optimal NN is selected as that having the minimum MSE. For a more general introduction to NN models and their implementation, we refer to reader to Bishop [2], and for details of PCA to Jolliffe [22]. We would like to point out that, while specialized custom NNs like those detailed in Takenaka et al. [54] are specialized and problem specific, our aim here is to outline a simpler and more accessible approach (based on MATLAB) that can be easily emulated by researchers studying solar radiation budgets and to help facilitate the development of new parameterizations of solar irradiance spectra in terms of cloud and aerosol parameters that can help reduce the uncertainty associated with their impact on planetary radiative forcing.

3.2. NN training

In this work we report on the training of two NN models – one with aerosol input parameters (for analysis of clear sky atmospheres), and one with cloud input parameters (for analysis of cloudy skies and atmospheric conditions). In each case, we performed a batch of runs on

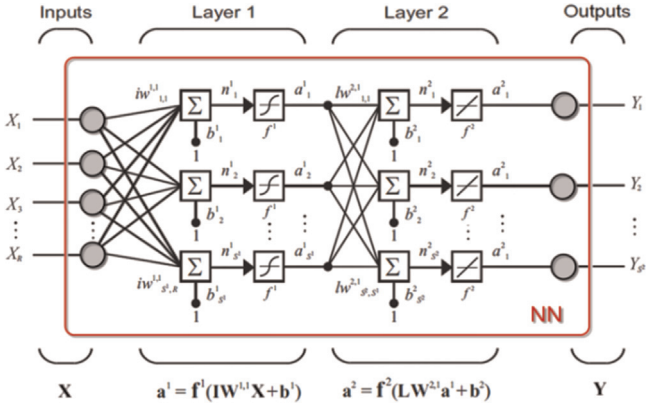

Fig. 2. Schematic showing the neural connectivity between input and output parameters.

Please cite this article as: Taylor M, et al. Neural network radiative transfer solvers for the generation of high resolution solar irradiance spectra parameterized by cloud and aerosol parameters. J Quant Spectrosc Radiat Transfer (2015), http://dx.doi.org/10.1016/j.jqsrt.2015.08.018

a grid of 100 NNs permuting through a range of architectures such that the number of hidden neurons ranged from 4–24 (in steps of 2) and so that the training proportion ranged from 40% to 90% (in steps of 5%). The NN connection weights and biases were then updated (i.e. trained) using an optimization learning algorithm. For each of these tests, 4 different optimization learning algorithms were investigated: the Levenberg–Marquardt (L–M) back-propagation optimization learning algorithm [29,31]: MATLAB flag "trainlm", Bayesian regularization: MATLAB flag "trainbr", resilient back-propagation: MATLAB flag "trainrp", and scaled conjugate-gradient back-propagation: MATLAB flag "trainscg". Details of the operation of back-propagation learning algorithms can be found in Rumelhart et al. [47]. For both the clear sky NN and the cloudy sky NN (see below), we found that the best results were obtained with the L–M algorithm. Training proceeded through a number of epochs until the MSE between NN outputs and the libRadtran targets (expected outputs) is minimized. In particular, the MSE obtained for each input–output vector in the validation proportion of the dataset was calculated for each NN in the grid. The optimal NN was then identified as the one whose architecture had the smallest validation MSE.

To train the clear sky NN, we extracted a subset of 2592 libRadtran input–output vectors from the clear sky LUT corresponding to a coarse but representative grid of runs spanning the parameter space: SZA=1:10:81, TOC=250:100:450, AOT=0:0.5:1.5, AE=0.2:0.6:2.0, SSA=0.7:0.2:0.9 and H2O=0.5:1.0:3.5, with each combination having an associated GHI (285:1:1050 nm). To train the cloudy sky NN, we extracted a subset of 1323 libRadtran input–output vectors from the cloudy sky LUT corresponding to a coarse but representative grid of runs: SZA=2:10:82, TOC=250:100:450, WCOT=0:5:30 and ICOT=0:5:30, with each combination having an associated GHI (285:1:2600 nm). In both cases, best results were obtained with 10 hidden neurons and a training: validation data ratio of 75%:25%. In relation to the evolution of NN performance with back-propagation epoch, the best validation MSE for the clear sky NN was 0.00015 (RMSE ≈ 0.01 W/m^2) after 20 training epochs (iterations) while the best validation MSE for the cloudy sky NN was 326.1 (RMSE ≈ 18.1 W/m^2) after 70 training epochs. Fig. 3 shows the progression of training for the cloudy sky NN where convergence has clearly been reached after 70 epochs at the horizontal asymptote for the best validation MSE. Note that the validation error curve, even after decades of epochs post-optimum training, does not increase. This signals both that a) training convergence has been achieved and b) over-fitting has been avoided.

4. Results

In order to test the (optimal) trained NNs described in Section 3.2, we created two test datasets (one for the clear sky NN and one for the cloudy sky NN) that spanned the full range of the training datasets, but which were constructed by randomly selecting 10,000 input–output vectors from each LUT so as to produce a finer grid of test runs. We wish to reiterate that, for each NN model, a large LUT is used twice – once for training and once for validation. For NN training a coarse grid spanning the full range of input parameter values was used so as to ensure that the NN was trained on a broad range of possible atmospheric conditions as represented by the 10,000 points in the multidimensional space of input–output data. Furthermore, during the validation stage, points

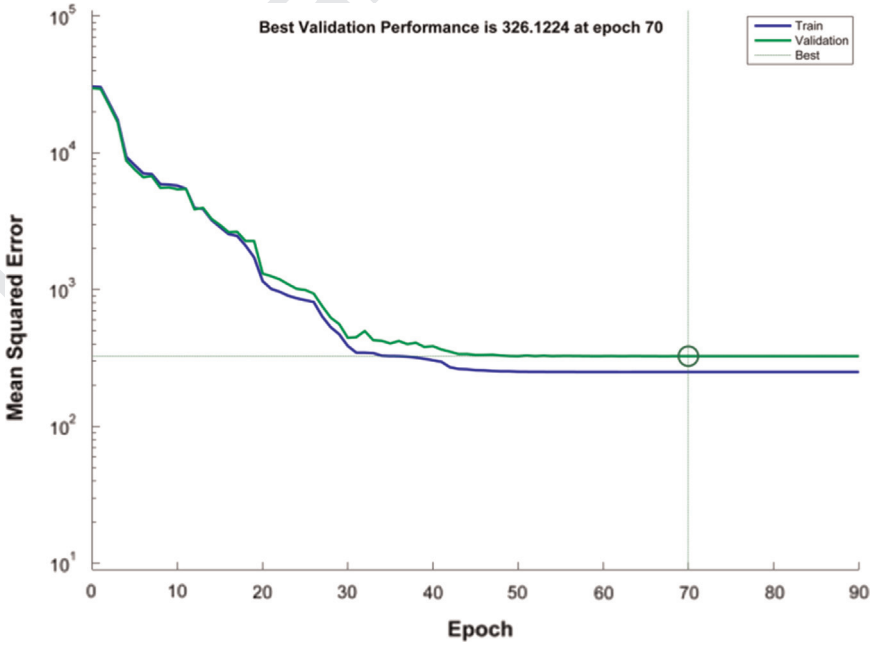

Fig. 3. Optimization of the cloudy sky NN. The MSE of the training data and validation data (100%-training %) with back propagation iteration (epoch) is shown for the optimal NN having 10 hidden neurons and a training: validation proportion of 75%:25%. For all NNs in the grid the goal for the back-propagation cost function was set to 1/100th of the total variance of the targets.

Please cite this article as: Taylor M, et al. Neural network radiative transfer solvers for the generation of high resolution solar irradiance spectra parameterized by cloud and aerosol parameters. J Quant Spectrosc Radiat Transfer (2015), http://dx.doi.org/10.1016/j.jqsrt.2015.08.018

that are coincident to both the training and validation samples were excluded so that, in essence, the validation space comprises a fine lattice spanning the LUT and overlaid (without coincident vertices) on a coarse lattice of training points. The coarse grid allows the NN to be general and is needed for the NN to be "accurate" in the sense of producing expected results for a wide range of input vectors. The fine grid tests the ability of the NN to interpolate to values near the points used to train the NN and therefore is a measure of its "precision". For implementation of this approach then, a full LUT is therefore necessary and is what gives our NN model its computational power. Once trained, the NN is able to function as an independent entity without the need for further reference to a LUT.

4.1. Testing the clear sky NN

Of the 10,000 randomly-selected runs to be used for testing the clear sky NN, 255 had input vectors that coincided with the 2592 input–output vectors of the training dataset and were eliminated, leading to a reduced set containing 9745 records. The input parameters were then fed to the trained clear sky NN to generate output spectra of the DNI, GHI, DHI and AF over the spectral window: 285–1050 nm. Fig. 4 visually shows the set of GHI spectra obtained with libRadtran and with the NN.

The spectra produced by libRadtran and those simulated by the NN were then integrated in order to assess the performance of the clear sky NN as shown in Fig. 5.

In Section 4.3 we will assess the average error and goodness of fit of the clear sky NN model. For now, we note that the spectrally-integrated GHI is very well modeled over the spectral range of PSR instruments considered here and for a large range of values of the integrated spectral irradiance resulting from differing atmospheric aerosol conditions. In order to investigate the impact of individual parameters on the spectra, we extracted records at the 10%, 25%, 50%, 75% and 90% quartiles of input parameter values in the random sample space. Fig. 6 shows the sensitivity of the NN fit to the libRadtran GHI spectra with AOT, SSA, SZA, TOC, H_2O and AE.

It is clear from Fig. 6 that the spectral GHI is not strongly sensitive to the level of atmospheric ozone (TOC) or columnar water vapor (H_2O). Some sensitivity to the level of H_2O is apparent in the near-IR part of the spectrum around 900–980 nm where water absorption is stronger. The solar irradiance decreases marginally with increasing AOT and increasing AE. A reverse trend is observed for the SSA. However, the GHI spectrum is highly sensitive to the SZA. The spectral maximum occurs at a wavelength $\approx$480 nm and decreases strongly in magnitude as the SZA increases from its 25% quartile value of 22° towards the zenith. In all cases, the NN is able to recover dominant absorption lines (e.g. at $\approx$420 nm, $\approx$690 nm, $\approx$760 nm, $\approx$840 nm, and $\approx$930 nm).

4.2. Testing the cloudy sky NN

Of the 10,000 randomly-selected runs comprising the subset of the cloudy sky LUT, 104 had input vectors which coincided with the 1323 input–output vectors of the dataset used to train the NN and were eliminated, leading

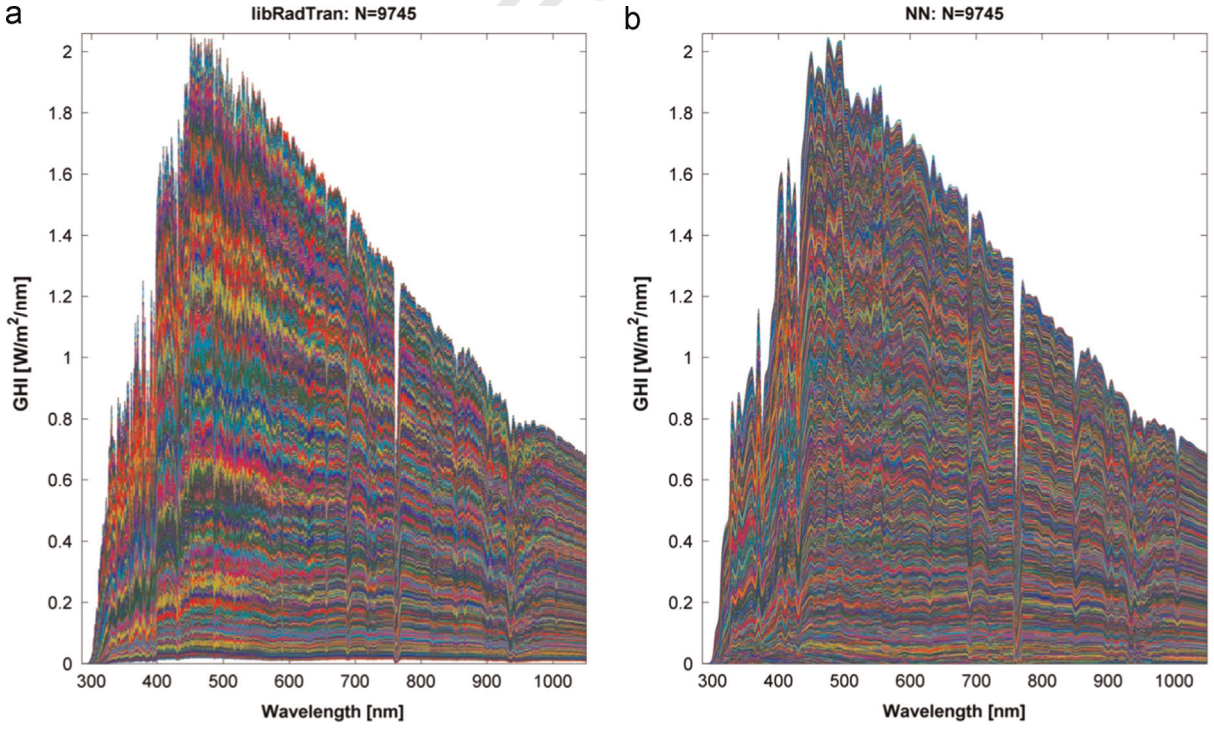

Fig. 4. *Left*: the 9745 randomly-selected GHI spectra produced by libRadtran. *Right*: the corresponding spectra produced by the NN solver. The spectral range for the clear sky NN is 285–1050 nm.

Please cite this article as: Taylor M, et al. Neural network radiative transfer solvers for the generation of high resolution solar irradiance spectra parameterized by cloud and aerosol parameters. J Quant Spectrosc Radiat Transfer (2015), http://dx.doi.org/10.1016/j.jqsrt.2015.08.018

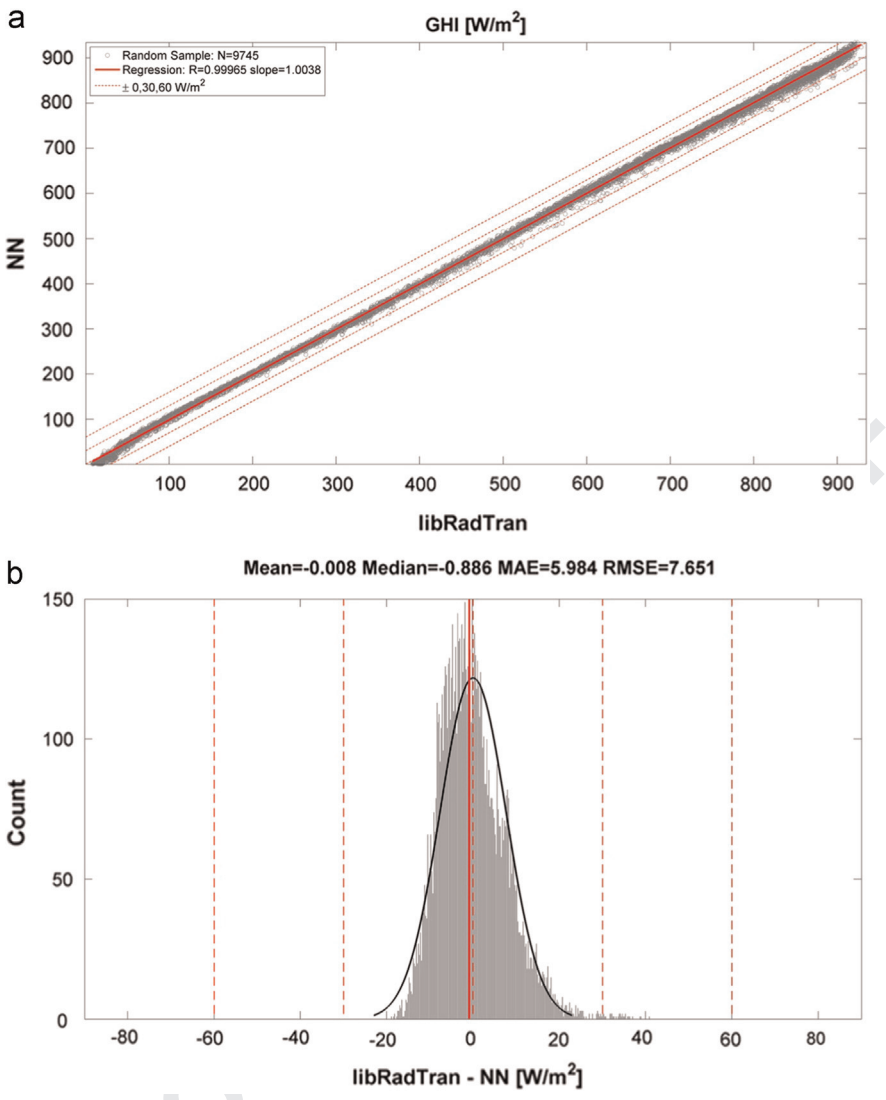

Fig. 5. (a) Scatterplot and linear regression of the 9745 randomly-selected and spectrally-integrated GHI spectra produced by the NN (*y*-axis) on the target libRadtran values (*x*-axis). (b) Histogram of the differences fit with a Gaussian distribution (black line). The mean difference is also shown (red line). Dotted red lines in both plots correspond to 0, ±30 and ±60 W/m^2 difference levels. (For interpretation of the references to color in this figure legend, the reader is referred to the web version of this article.)

to a reduced set containing 9896 data points. While it is generally not good practice to remove outliers (since they often correspond to interesting phenomena), in relation to the development of NN models, it is important that data values that are infrequently-occurring or which fall outside the problem domain, are removed as they can significantly bias the assessment of NN performance. This led us to study the input–output vector data in more detail. The random sample revealed that a small sub-sample of the GHI spectra (108 data points) presented uncharacteristic ("irregular") trends with very sharp high irradiance peaks in the near-infrared part of the spectrum, suppression of the GHI in the visible and ultraviolet parts of the spectrum, and again in the mid-infrared. These irregular spectra were associated with the specific combination of conditions: SZA $\geq 88^\circ$ concurrent with ICOT ≥ 17 and were eliminated from the test sample, leading to a reduced set containing 9788 data points. The input parameters were then fed to the trained clear sky NN to generate output spectra of the GHI over the spectral window: 285–2600 nm. Fig. 7 visually shows the set of GHI spectra obtained with libRadtran and with the NN.

We report the following macro-statistics to assess the performance of the cloudy sky NN: (i) the sample bias as a measure of systematic error, (ii) the root mean squared error (RMSE) as a measure of dispersion, and (iii) the Pearson product–moment correlation coefficient as a regression measure. Fig. 8 shows that the correlation coefficient calculated by regressing NN outputs on libRadtran targets was found to be $R=0.991$ (with slope ≈ 0.97), the sample bias was found to be: -0.076 W/m^2 and the RMSE$=7.767$ W/m^2. In particular, only 394 of the $N=$ 9788 data points (4.03% of the random sample) are marginally outside the ±60 W/m^2 band; the majority (

Please cite this article as: Taylor M, et al. Neural network radiative transfer solvers for the generation of high resolution solar irradiance spectra parameterized by cloud and aerosol parameters. J Quant Spectrosc Radiat Transfer (2015), http://dx.doi.org/10.1016/j.jqsrt.2015.08.018

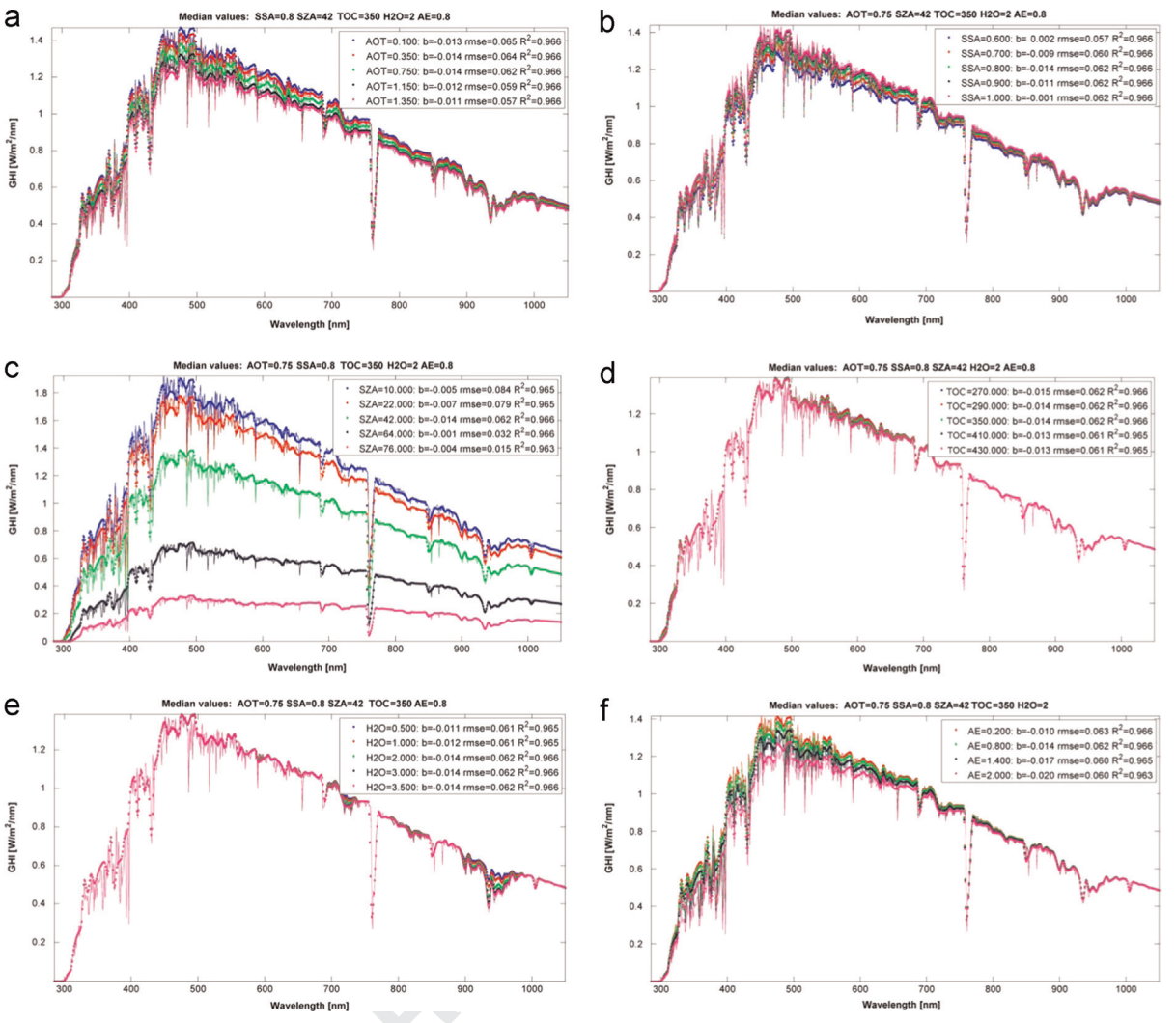

Fig. 6. Quartile trends of the spectral GHI with (a) AOT, (b) SSA, (c) SZA, (d) TOC, (e) H2O and (f) AE. The libRadtran data is shown by the dots while the NN model is represented by lines. For each case, the bias *b*, the *RMSE* and the coefficient of determination R^2 are presented. For case (f), the 10% and 25% quartiles coexist at AE=0.2.

9394 of the $N=$ 9788 data points or 95.97%) of the NN model outputs are well within $\pm$0–60 W/m^2 band of the libRadtran simulated target values. These initial results suggest that the optimal cloudy sky NN is generally well trained and performing properly the function approximation between input and output vectors.

In Section 4.3 we will assess the average error and goodness of fit of the cloudy sky NN model in detail. In what follows, we investigate the dependence of the irradiance spectrum on variations in the values of the NN model inputs. Fig. 9 shows the sensitivity of the NN fit to the libRadtran GHI spectra with WCOT, ICOT, SZA and TOC. It is clear from Fig. 9 that the spectral GHI is not sensitive to the level of atmospheric ozone. There is an expected drop in solar irradiance with COT (both ice and water), and with SZA. Importantly, the GHI appears to be insensitive to the level of total columnar ozone (TOC).

In next section, we analyze the size of average errors and goodness of fit measures for both the clear sky NN and for the cloud sky NN models with a view to providing an assessment of their quality and performance in terms of accuracy and precision.

4.3. Assessment of the performance of the NN models

In Table 2 we summarize the goodness of fit statistics associated with the differences between the values of the integrated spectra for both the clear sky NN and the cloud NN.

In the case of the cloudy NN for example, the proportion of points above the 30 W/m^2 difference level is 532/9788 or 5.44%. It is useful to check that the minimum RMSE at this level given by $\sqrt{[(5.44/100)*30^2]}=6.99$ W/m^2 is well below the value of RMSE=18.067 W/m^2 for the whole sample of $N=9788$ points, which is the case. The same is true for the 150/9788 or 1.53% of points above the 60 W/m^2 level where the minimum RMSE given by $\sqrt{[(1.53/100)*30^2]}=3.71$ W/m^2 again is well below the value of RMSE for the whole sample. Similarly, for the case

Please cite this article as: Taylor M, et al. Neural network radiative transfer solvers for the generation of high resolution solar irradiance spectra parameterized by cloud and aerosol parameters. J Quant Spectrosc Radiat Transfer (2015), http://dx.doi.org/10.1016/j.jqsrt.2015.08.018

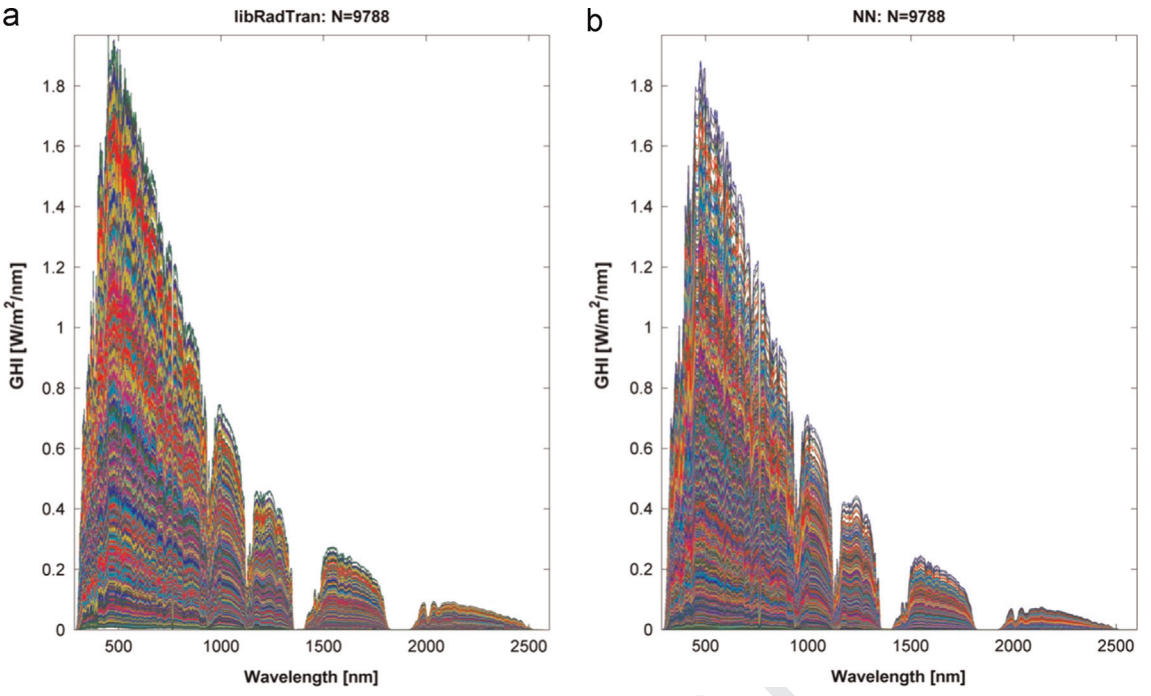

Fig. 7. *Left*: the 9788 randomly-selected GHI spectra produced by libRadtran. *Right*: the corresponding spectra produced by the NN solver.

of the clear sky NN (where the agreement is stronger as can be seen in the upper panel of Fig. 5, the proportion of points above the 30 W/m^2 is accordingly much lower at 34/9745 or 0.35% and the minimum RMSE given by $\sqrt{[(0.35/100)*30^2]}=1.77$ W/m^2 is well below the value of RMSE=7.65 W/m^2 for the whole sample of $N=9745$ points. In this particular case, there are no points where the difference is in excess of 60 W/m^2. Note that we have followed the standard practice (Willmott et al, 1985) of assuming that the reference values (libRadtran simulated output spectra) used to valid our model (NN output spectra) have zero error. While it has not yet been possible to associate an error with target spectra produced by libRadtran, it is worth trying to place the performance of such radiative transfer codes in context by understanding the general uncertainty associated with them. Band-integrated irradiances have been reported to be as low as 1% for spectrally-integrated cases such as short- and long-wave fluxes at the top of the atmosphere and/or at the surface [15]. In their presentation of the results of inter-comparison of radiative transfer codes that use line-by-line calculation rather than band-integration, Oreopoulos and Mlawer [39] also quote an uncertainty of the order 1% for these fluxes at specific solar zenith angles and cloud-free conditions. An important study by Ineichen [20], that evaluated the performance of 8 high performance clear sky solar irradiance models against a set of 16 independent datasets covering 20 years/stations, found that the accuracy of these models for the GHI using the RMSE as a measure was of the order ≈4–5% (or ≈19–23 W/m^2) for mostly clear sky conditions [20]. These studies provide a useful guide and general context for the evaluation of the performance of our NN models using goodness of fit statistics presented above.

With regard to considerations of speed, we have compared the NN model runtime with the libRadtran simulation runtime for production of the 10,000 output spectra used for validation for both the clear sky and cloudy sky cases. As an indication, with a single batch process on a quad-core PC, the clear sky libRadtran simulation involving 6 input parameters and spanning the spectral range 285–1050 nm requires ≈200 h while the cloudy sky libRadtran simulation involving 4 input parameters but spanning the spectral range 285–2600 nm requires ≈235 h (to the nearest hour). The clear sky NN requires 0.916 s and the cloudy NN requires 0.714 s. Clearly, for real-time mapping applications at the national scale where the number of pixels is typically of the order ≈10^4–10^5 then radiative-transfer simulations are computationally too slow and the NN is greatly advantageous, allowing maps to be produced well within a 1-min timescale. This makes the NN practical for application to high spatial resolution cloud data maps and possibly for the development of forecast models since cloud maps from weather satellites like MSG3 are produced at 15-min intervals. The clear sky and cloudy sky NN solvers are capable of taking continuous data directly as input and instantaneously generating the spectral GHI accurately. In the next section we show how the cloudy sky NN can be applied to real-time satellite cloud data.

4.4. Real-time application using satellite cloud data

In this section, we apply the cloudy sky NN solver to real cloud parameter data from the geostationary satellite MSG3 (see Section 2.2) over a region of interest (ROI): Greece which spans an area from 34°N to 43°N latitude and 19°E to 29°E longitude. MSG3–SEVIRI cloud phase flags (0=clear sky, 1=water cloud, 2=ice cloud, and 3=mixed cloud) and associated ICOT and WCOT values

Please cite this article as: Taylor M, et al. Neural network radiative transfer solvers for the generation of high resolution solar irradiance spectra parameterized by cloud and aerosol parameters. J Quant Spectrosc Radiat Transfer (2015), http://dx.doi.org/10.1016/j.jqsrt.2015.08.018

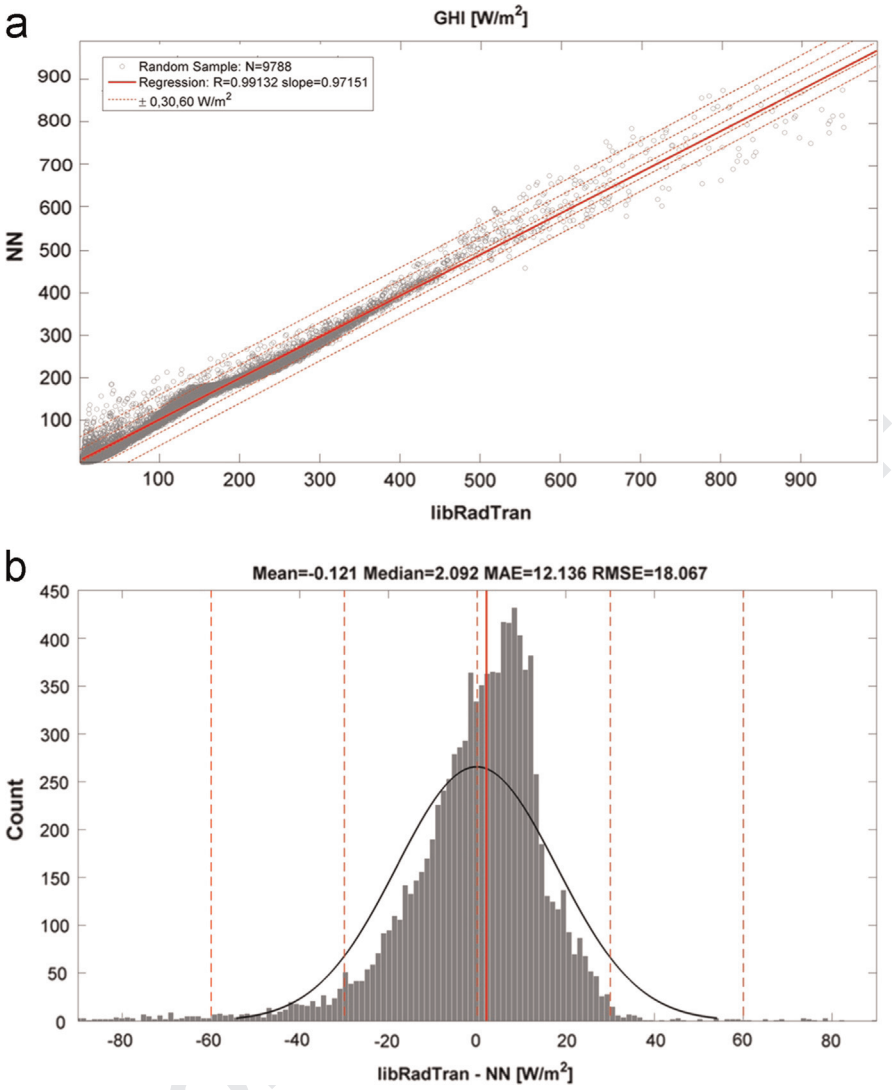

Fig. 8. (a) Scatterplot and linear regression of the 9788 randomly-selected and spectrally-integrated DHIGHI spectra produced by the NN (*y*-axis) on the target libRadtran values (*x*-axis), together with the 0, ±30 and ±60 W/m^2 bands (red dotted lines). (b) Histogram of the differences fit with a Gaussian distribution (black line). The mean difference is also shown (red line). (For interpretation of the references to color in this figure legend, the reader is referred to the web version of this article.).

were extracted for each of 54,531 pixels ($\approx 0.05^\circ \times 0.05^\circ$) in the 2D stereoscopically-rotated map of the ROI on the 4th of June 2014 at 07:30am UGT. The resultant COT map for the ROI is shown in Fig. 10(b). To this data, the SZA in each pixel together with a constant climatological value of TOC=350DU, was appended to form a matrix of 54,531 row vectors (one for each pixel) having 6 columns: latitude, longitude, ICOT, WCOT, SZA and TOC. Sub-matrices (excluding latitude and longitude entries) were then fed to the trained cloudy sky NN and the GHI was generated and spectrally-integrated for each input vector/ pixel resulting in Fig. 10(d). In order to provide an assessment of the underlying clear sky GHI map, a replica of the input matrix was made with all ICOT and WCOT values set to 0 and fed to the cloudy sky NN to produce "clear sky" GHI spectra which were also integrated for each pixel. The NN-calculated clear sky spectrally-integrated GHI is shown in Fig. 10(a). Close observation of these images illustrates that the map of integrated GHI for cloudy skies (the general case) in Fig. 10(d) results from the modulation of the "clear sky" GHI map of Fig. 10(a) by the map of COT in Fig. 10(b). A quantitative measure of this is the clear sky factor (CSF) which is calculated by integrating the spectral GHI in the presence of clouds and normalizing it to the value of the integrated spectral GHI for clear sky conditions (i.e. ICOT=WCOT≡0):

$$\mathrm{CSF} = \frac{\int_{\lambda_1}^{\lambda_2} \mathrm{GHI}(\mathrm{ICOT}, \mathrm{WCOT}, \lambda) d\lambda}{\int_{\lambda_1}^{\lambda_2} \mathrm{GHI}(0, 0, \lambda) d\lambda} \tag{7}$$

As such, the CSF ranges from [0, 1] such that CSF=1 corresponds to the clear sky case. The map of the CSF for

Please cite this article as: Taylor M, et al. Neural network radiative transfer solvers for the generation of high resolution solar irradiance spectra parameterized by cloud and aerosol parameters. J Quant Spectrosc Radiat Transfer (2015), http://dx.doi.org/10.1016/j.jqsrt.2015.08.018

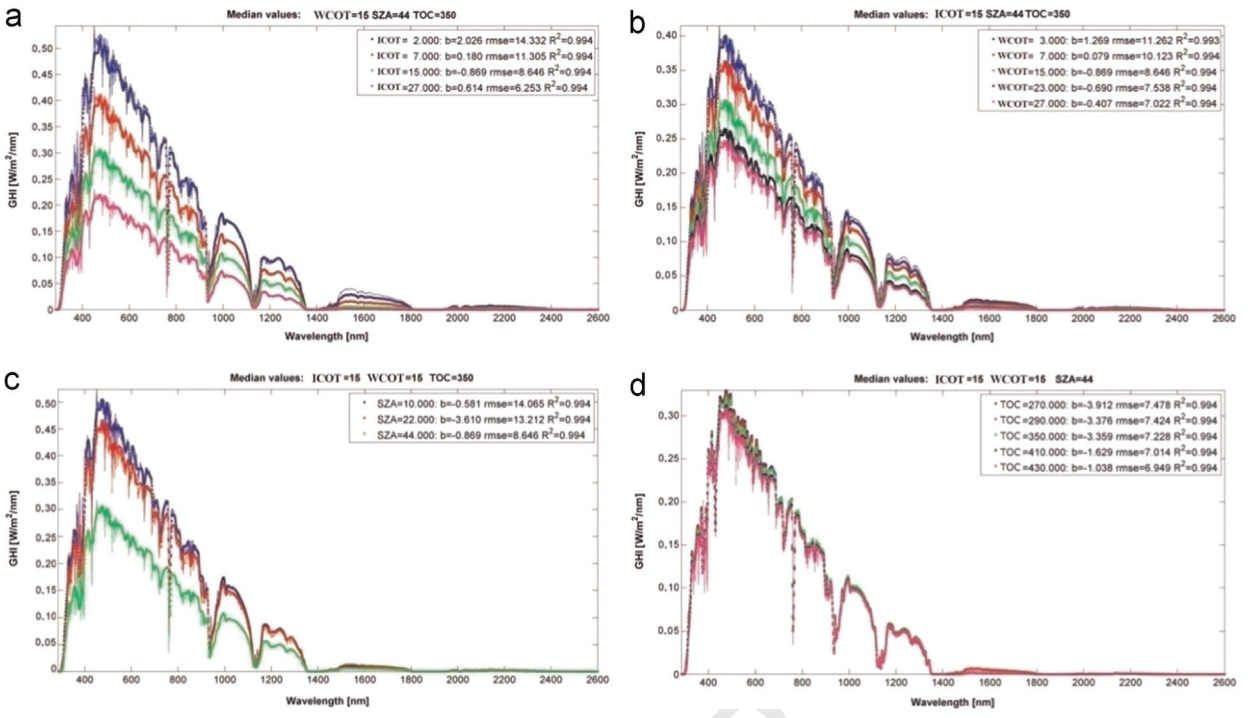

Fig. 9. Quartile trends of the spectral GHI with (a) ICOT, (b) WCOT, (c) SZA and (d) TOC. The libRadtran data is shown by the dots while the NN model is represented by lines. For each case, the bias b, the RMSE and the coefficient of determination R^2 are presented.

Table 2
Goodness of fit statistics associated with the differences between the values of the integrated spectra for both the clear sky NN and the cloud NN.

	Clear sky NN	Cloudy NN
N	9745	9788
b [W/m^2]	−0.01	−0.12
MAE [W/m^2]	5.98	12.14
RMSE [W/m^2]	7.65	18.07
N (0 < difference ≤ 30 W/m^2)	9711 (99.65%)	9256 (94.56%)
N (30 < difference ≤ 60 W/m^2)	34 (0.35%)	382 (3.90%)
N (difference > 60 W/m^2)	0	150 (1.54%)

the ROI calculated in this way is shown in Fig. 10(c). In reality, as we have shown, the GHI is also a function of SZA (to a major extent) and TOC (to a minor extent). In the context of more general real-time pixel maps of the spectrally-integrated GHI over a ROI, one should picture maps of the actual spectrally-integrated GHI as resulting from the product of 2 maps: the first, corresponding to a map of the spectrally-integrated clear sky GHI and the second, being a map of the CSF. The reason that this interpretation (in terms of the effect of clouds only) is valid is because the integrated spectral GHI is insensitive to TOC. In addition, the SZA is a constant of the solar position (i.e. local time and geolocation) and therefore there exists an inertial frame of reference (siderial time) where the spectral GHI is also independent of SZA. The CSF is the normalized and spacetime-invariant manifestation of the spectrally-integrated actual GHI. As a further assessment of the performance capability of the cloudy sky NN, 54,531 libRadtran simulations (one for each pixel) corresponding to the matrix of input vectors were used to generate GHI spectra which were then integrated to produce the map in Fig. 10(e). The PFE calculated from the difference of the spectrally-integrated GHI calculated with the cloudy sky NN and with libRadtran is shown in Fig. 10(f).

There is strong visual agreement between the NN-calculated spectrally-integrated GHI map of Fig. 10(d) and that derived from libRadtran simulated spectra in Fig. 10 (e). Two key observations can be made: i) regions of GHI below ≈ 400 W/m^2 in both maps correspond, as expected, to regions of high COT above ≈ 30 (i.e. dominated by the presence of thick cloud) and ii) clear sky regions where COT is less than ≈ 5 have slightly higher values of GHI when calculated with libRadtran (≈ 700 W/m^2) compared with the cloudy sky NN (≈ 600 W/m^2). This latter finding is observable in the PFE "difference map" of Fig. 10 (f) where the cloudy sky NN is seen to under-estimate "clear sky" regions (PFE ≈ +15% to +20%) and over-estimate the regions of dense cloud (PFE ≈ −10% to −15%). In Fig. 11 the spectrally-integrated GHI obtained with the cloudy sky NN and that derived from libRadtran spectra using the same inputs in all 54,531 pixels of the ROI are plotted.

For the cyan region (COT > 30) and the blue region (COT ≤ 5) of Fig. 11, the level of correlation shows a marked dependence on the magnitude integrated solar irradiance. In particular, the cloudy sky NN underestimates for COT ≤ 5 and slightly overestimates for COT > 30. The overestimation for COT > 30 reaches ≈ 30 W/m^2. Indeed, Up to a value of ≈ 550 W/m^2 the difference in the spectrally-integrated GHI lies within the ± 30 W/m^2 error

Please cite this article as: Taylor M, et al. Neural network radiative transfer solvers for the generation of high resolution solar irradiance spectra parameterized by cloud and aerosol parameters. J Quant Spectrosc Radiat Transfer (2015), http://dx.doi.org/10.1016/j.jqsrt.2015.08.018

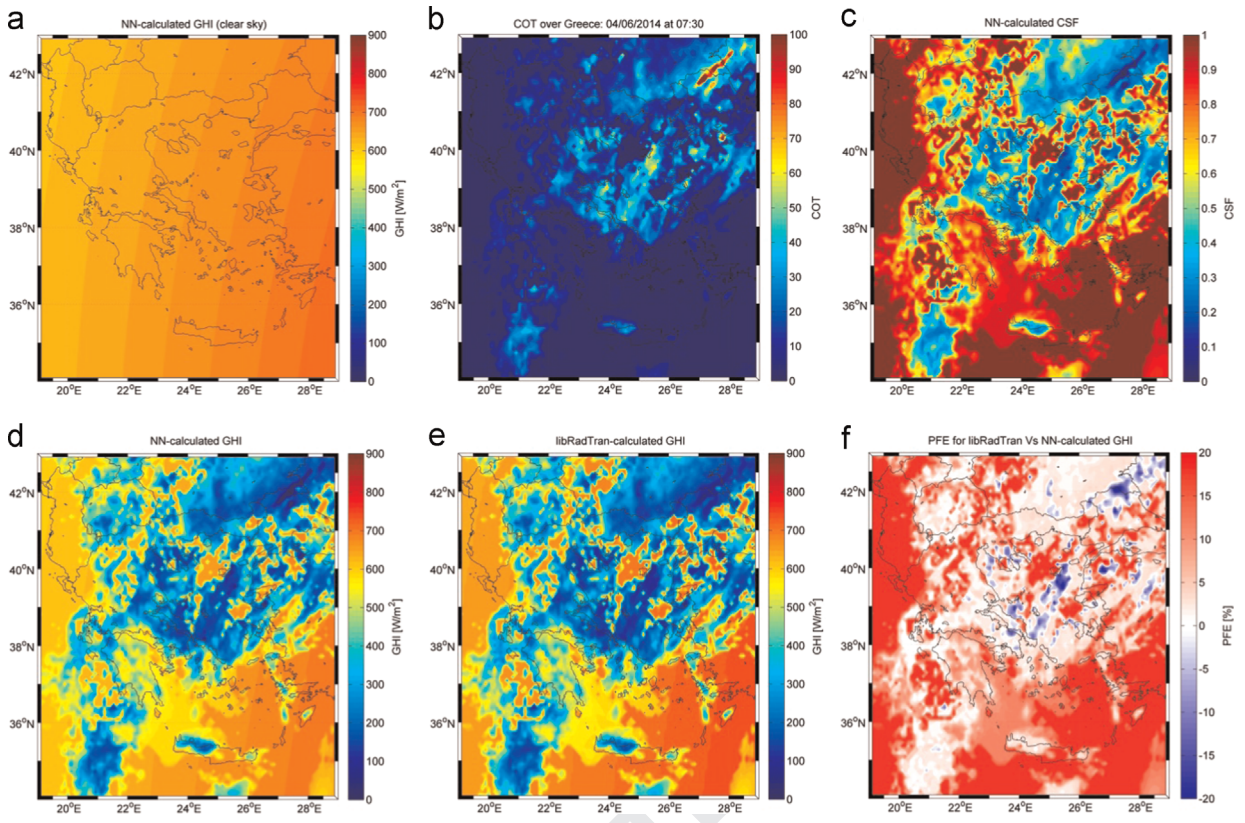

Fig. 10. (a) The spectrally-integrated "clear sky" GHI map for the ROI (54,531 pixels) at 07:30am UGT. Note that, at this time of the morning in Greece, the sun is situated nearly due East. (b) The COT map obtained from MSG3 satellite measurements of ICOT and WCOT by the SEVIRI instrument and associated cloud products. (c) The CSF map. (d) The spectrally-integrated GHI map generated by the cloudy sky NN. (e) The spectrally-integrated GHI map generated by libRadtran for the same inputs. (f) The PFE resulting from the difference between the spectrally-integrated GHI map generated by libRadtran and the cloudy sky NN.

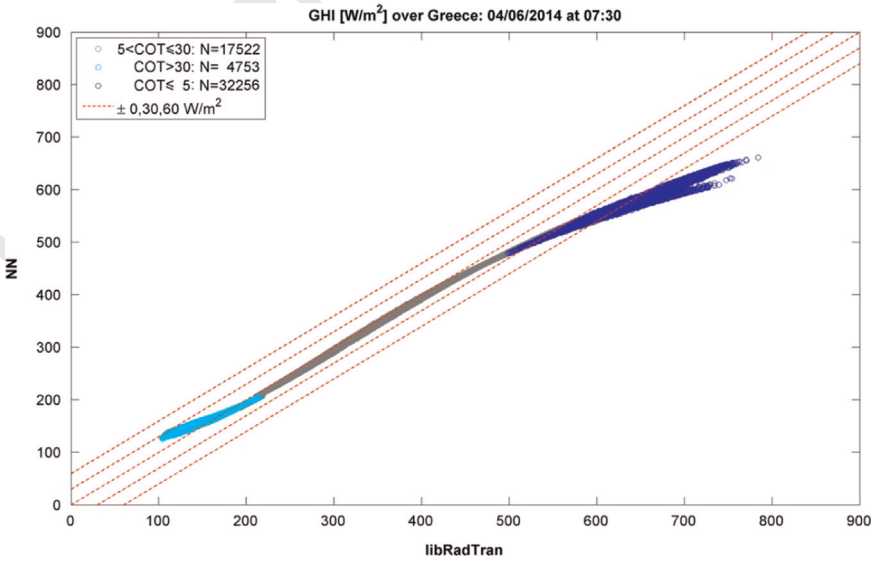

Fig. 11. A scatter plot of the spectrally-integrated GHI calculated from libRadtran (*x*-axis) and cloud sky NN spectra (*y*-axis) for the 54,531 pixels of the ROI color-coded for three different behaviors of the performance of the cloudy sky NN with respect to libRadtran: i) "linear" ($5 < COT \leq 30$), ii) "over-estimation" ($COT > 30$) and iii) "under-estimation" ($COT \leq 5$). The red dotted lines correspond to the 0, ± 30 and ± 60 W/m^2 bands. (For interpretation of the references to color in this figure legend, the reader is referred to the web version of this article.)

Please cite this article as: Taylor M, et al. Neural network radiative transfer solvers for the generation of high resolution solar irradiance spectra parameterized by cloud and aerosol parameters. J Quant Spectrosc Radiat Transfer (2015), http://dx.doi.org/10.1016/j.jqsrt.2015.08.018

band. Above this level of solar radiation, the cloudy sky NN under-estimates the spectrally-integrated GHI compared to libRadtran, leading to an increase in the value of the average difference as atmospheric conditions approach purely clear skies where $COT \equiv 0$. Since the lowest spectrally-integrated GHI values occur at high COT values, the impact of the overestimation is not of such importance in solar energy applications where the surface integrated solar irradiance is low. For clear sky pixels at low COT values is more pronounced and exceeds 60 W/m^2. This has to do with the limited ability of the cloudy NN to accurately model clear sky conditions. The aim, however, of this paper is to demonstrate a new methodology for deducing solar radiation spectra from aerosol and cloud inputs using neural networks and to assess the sensitivity of the models to variations in the input parameters. This work is a first step to support the development of holistic systems that are valid for both cloudy and clear sky conditions in the presence of aerosol.

In Table 3 we investigate the dependence of the size of the average error with COT using an exponential scale.

According to the findings of Table 3, average error statistics are within ± 30 W/m^2 for low to high levels of COT above ≈ 4 with an optimum error ≈ 5 W/m^2 for cloud conditions corresponding to the interval $8 < COT \leq 16$. The average error increases exponentially as condition approaches pure clear skies being of the order 113 W/m^2 for the interval $0 < COT \leq 1$. We wish to reiterate here that the COT is a derived parameter in the cloud data algorithm used by MSG3 and is sensitive to non-uniformity of cloud features in the SEVIRI field of view. In the near future we will validate the results presented here against in situ measurements from precision solar radiometers (PSR) and other instruments in the National Observatory of Athens (NOA) solar radiation network, as well as simulations provided by NOA's operational forecasting numerical weather prediction model (MM5).

Finally in this section, in addition to the statistical analysis of the differences between the spectrally-intergrated GHI obtained from spectra produced by the cloudy sky NN and libRadtran, we also calculated the structural similarity index for maps (SSIM) developed by Wang et al. [57] to assess agreement in morphological detail between 2 images/maps. The SSIM has values in the range [0, 1] with unity corresponding to perfect morphological similarity. For the 54,531 pixel maps of Fig. 10 (d) and (e), we obtained the value: SSIM=0.91 when a Gaussian window of size 10 pixels was used, suggesting a strong degree of structural similarity despit the fact that the RMSE for clearest sky pixels ($0 \leq COT \leq 1$) is of the order of ≈ 113 W/m^2. The analysis above performed with reference to radiative transfer simulations suggest that the cloudy sky NN has the potential to produce irradiance spectra whose spectrally-integrated GHI values that are accurate for the majority of realistic cloud conditions and spatially-robust in terms of solar irradiance features.

Conclusion

In this paper, we report on the development of NN solvers for estimation of solar irradiance spectra based on clear sky (aerosol) parameters and cloudy sky parameters. To accomplish this, a large (2.4 million record) LUT of DNI, GHI, DHI and AF irradiance as a function of ICOT, WCOT, TOC, SZA AOT, SSA, AE and H_2O was generated with libRadtran. Two feed-forward NN solvers were trained and tested on a broad range of $\approx$10,000 randomly-selected records that smoothly span a large input parameter space for both clear sky and cloudy sky conditions. The NN solvers, once trained, are fast and accurate, and offer new parameterizations of clear sky and cloudy atmospheres. In particular, the application of the clear sky NN solver to an array of parameters including: AOT, SSA, SZA, TOC, H2O and AE revealed that solar spectra are most sensitive to the SZA and that the effect of TOC on the spectral GHI, for example, is small. These two effects were also found to be true in the context of cloudy skies.

The cloudy sky NN solver for the GHI has a spectral resolution of 1 nm over the range of wavelengths 285–2600 nm and is capable of producing maps of spectrally-integrated GHI of the order of 10^4–10^5 pixels within 1-min and with relative errors less than 20% of libRadtran-simulated values. Application of the cloudy sky NN solver to satellite cloud data (cloud optical thickness, cloud type and cloud phase) extracted and stereoscopically-rotated for the Greek region from MSG3–SEVIRI, was straightforward, rapid, and provided coherent results that could be interpreted in terms of the clear sky factor. Work is in progress to elucidate the multiparametric dependence of the CSF on a fuller set of aerosol and cloud parameters. The development of NN solvers that account for some particle mixing (e.g. cloud and aerosol internal/external mixing or mixing of aerosol types, nonspherical shape) using methodologies like the one presented here, will help open the door to new simulations of these important interactions

Table 3
The average error associated with the difference between NN-calculated and libRadtran calculated spectrally-integrated GHI as a function of increasing COT (in powers of 2).

	N	*N* (cumulative) (%)	*b* [W/m^2]	MAE [W/m^2]	RMSE [W/m^2]
$0 < COT \leq 1$	22,239	40.8	113.67	113.67	113.86
$1 < COT \leq 2$	1310	43.2	90.60	90.60	90.95
$2 < COT \leq 4$	7200	56.4	68.27	68.27	69.87
$4 < COT \leq 8$	4843	65.3	22.22	22.22	24.63
$8 < COT \leq 16$	6815	77.8	5.00	5.00	5.67
$16 < COT \leq 32$	8234	92.9	6.99	7.0	7.18
$COT > 32$	3890	100.0	−6.66	8.35	10.87

Please cite this article as: Taylor M, et al. Neural network radiative transfer solvers for the generation of high resolution solar irradiance spectra parameterized by cloud and aerosol parameters. J Quant Spectrosc Radiat Transfer (2015), http://dx.doi.org/10.1016/j.jqsrt.2015.08.018

and their impact on radiation budgets. It is hoped that the fast and accurate, clear sky and cloudy sky NN solvers presented here are an initial step in this direction and will help facilitate studies of the impact of aerosol and cloud parameters on solar irradiance spectra at the local, regional or global scale, important to improving our understanding of the Earth's radiation budget.

Uncited references

[18',44].

Acknowledgments

The authors would like to thank the anonymous reviewers for their comments that significantly improved the technical level and presentation of the submitted manuscript as well as the Editor-in-Chief Michael I. Mishchenko for his professional handling of the peer review.

References

[1] Allan RP, Ringer MA, Pamment JA, Slingo A. Simulation of the Earth's radiation budget by the European centre for medium-range weather forecasts 40-year reanalysis (ERA40). J Geophys Res 2004;109: D18107.
[2] Bishop CM. Neural networks for pattern recognition. New York, USA: Oxford University Press; 1995.
[3] Boucher O, Randall D, Artaxo P, Bretherton C, Feingold G, Forster P, Kerminen V-M, Kondo Y, Liao H, Lohmann U, Rasch P, Satheesh SK, Sherwood S, Stevens B, Zhang XY. Clouds and aerosols. In: Stocker TF, Qin D, Plattner G-K, Tignor M, Allen SK, Boschung J, Nauels A, Xia Y, Bex V, Midgley PM, editors. Climate Change 2013: the physical science basis. Contribution of working group I to the fifth assessment report of the intergovernmental panel on climate change. United Kingdom and New York, NY, USA: Cambridge University Press, Cambridge; 2013.
[4] Cameron C, Windmeijer A, Frank AG, Gramajo H, Cane DE, Khosla C. An *R*-squared measure of goodness of fit for some common nonlinear regression models. J Econ 1997;77(2):1790–2.
[5] Cole JNS, Barker HW, Randall DA, Khairoutdinov MF, Clothiaux EE. Global consequences of interactions between clouds and radiation at scales unresolved by global climate models. Geophys Res Lett 2005;32:L06703. http://dx.doi.org/10.1029/2004GL020945.
Q5 [6] Cybenko G. Approximation by super-positions of a sigmoidal function. Math Control Signals Syst 1989;2:303–14.
[7] Dahlback A, Stamnes K. A new spherical model for computing the radiation field available for photolysis and heating at twilight. Planet Sp Sci 1991;39:671–83.
Q6 [8] Demuth H, Beale M. Neural network toolbox for use with MATLAB. Mathworks; .
[9] Derrien M, Le Gleau H. MSG/SEVIRI cloud mask and type from SAFNWC. Int J Remote Sens 2005;26:4707–32. http://dx.doi.org/10.1080/01431160500166128.
[10] Dorvlo ASS, Jervase JA, Lawati Ali Al. Solar radiation estimation using artificial neural networks. Appl Energy 2002;71:307–19.
[11] Egorova T, Rozanov E, Manzini E, Haberreiter M, Schmutz W, Zubov V, Peter T. Chemical and dynamical response to the 11-year variability of the solar irradiance simulated with a chemistry-climate model. Geophys Res Lett 2004;31:6.
[12] Ellingson RG, Ellis J, Fels S. The intercomparison of radiation codes used in climate models: longwave results. J Geophys Res 1991;96: 8929–53.
[13] Fu Q, Liou K-N. On the correlated *k*-distribution method for radiative transfer in nonhomogeneous atmosphere. J Atmos Sci 1992;49: 2139–56.
[14] Gasca M, Sauer T. Polynomial interpolation in several variables. Adv Comput Math 2000;12:377–410.
[15] Gasteiger J, Emde C, Mayer B, Buras R, Buehler SA, Lemke O. Representative wavelengths absorption parameterization applied to satellite channels and spectral bands. J Quant Spectrosc Radiat Transf 2014;148:99–115.
[16] Haberreiter M, Schmutz W, Hubeny I. Astron Astrophys 2008;492: 833.
[17] Hess M, Koepke P, Schult I. Optical properties of aerosols and clouds: the software package OPAC. Bull Am Meteorol Soc 1998;79(5): 831–44.
[18] Hu YX, Stamnes K. An accurate parameterization of cloud radiative properties suitable for climate modeling. J Clim 1993;6:728–42.
[19] Hu YX, Stamnes K. Climate sensitivity to cloud optical properties. Tellus B 2000;52(1). http://dx.doi.org/10.3402/tellusb.v52i1.16084.
[20] Ineichen P. Comparison of eight clear sky broadband models against 16 independent data banks. Sol Energy 2006;80(4):468–78.
[21] Intergovernmental Panel on Climate Change (IPCC). Climate change 2013: the physical science basis: contribution of the working group I to the fifth assessment report of the IPCC. New York: Cambridge University Press; 2013.
[22] Jolliffe IT. Principal component analysis. 2nd ed.New York: Springer; 2002.
[23] Kahn RA. Reducing the uncertainties in direct aerosol radiative forcing. Surv Geophys 2012;33(3–4):701–21.
[24] Kato S, Ackerman T, Mather J, Clothiaux E. The *k*-distribution method and correlated-*k* approximation for shortwave radiative transfer model. J Quant Spectrosc Radiat Transf 1999;62:109–21.
[25] Kneizs FX, Shettle EP, Gallery WO, Chetwynd JH, Abreu LW, Selby JEA, Clough SA, Fenn RW. Atmospheric transmittance/radiance: computer code LOWTRAN 6.Report AFGL-TR-83-0187. Hanscom AFB, MA: Air Force Geophysics Laboratroy; 1983.
[26] Koren I, Remer LA, Kaufman YJ, Rudich Y, Martins JV. On the twilight zone between clouds and aerosols. Geophys Res Lett 2007;34: L08805.
[27] Kurucz RL, Rabin DM, Jefferies JT. Synthetic infrared spectra. In: Proceedings of IAU symposium on infrared solar physics. Kluwer Academic Norwell, MA, USA. vol. 154; 1992.
[28] Lesins G, Chylek P, Lohmann U. A study of internal and external mixing scenarios and its effect on aerosol optical properties and direct radiative forcing. J Geophys Res 2002;107(D10): 4094. http://dx.doi.org/10.1029/2001JD000973.
[29] Levenberg K. A method for the solution of certain non-linear problems in least squares. Q J Appl Math 1944;2:164–8.
[30] Lopez G, Rubio MA, Martinez M, Batlles FJ. Estimation of hourly global photosynthetically active radiation using artificial neural network models. Agric For Meteorol 2001;107:279–91.
[31] Marquardt D. An algorithm for least-squares estimation of nonlinear parameters. J Soc Ind Appl Math 1963;11:431–41.
[32] Mayer B, Kylling A. Technical note: the libRadtran software package for radiative transfer calculations-description and examples of use. Atmos Chem Phys 2005;5:1855–77.
[33] McClatchey RA, Fenn RW, Selby JEA, Volz FE, Garing JS. Optical properties of the atmosphere. Report AFCRL-72-0497. 3rd ed.Air Force Cambridge Research Laboratories; 1972.
[34] MétéoFrance. Algorithm theoretical basis document for cloud products (CMa-PGE01 v3.2, CT-PGE02 v2.2 & CTTH-PGE03 v2.2).Technical Report SAF/NWC/CDOP/MFL/SCI/ATBD/01. Paris: MétéoFrance; 2013.
[35] Nakajima T, Tanaka M. Matrix formulations for the transfer of solar radiation in a plane-parallel scattering atmosphere. J Quant Spectrosc Radiat Transf 1986;35:13–21.
[36] Nakajima T, Tanaka M. Algorithms for radiative intensity calculations in moderately thick atmospheres using a truncation approximation. J Quant Spectrosc Radiat Transf 1988;40:51–69.
[37] Norris JR, Slingo A. Trends in observed cloudiness and Earth's radiation budget: what do we not know and what do we need to know? In: Heintzenberg J, Charlson RJ, editors. Clouds in the perturbed climate system: their relationship to energy balance, atmospheric dynamics, and precipitation. Cambridge, MA: MIT Press; 2009. p. 17–36.
Q8 [38] Nyamsi W, Espinar B, Blanc P, Wald L. How close to detailed spectral calculations is the k-distribution method and correlated-*k* approximation of Kato et al. (1999) in each spectral interval? Meteorol Z 2014.
[39] Oreopoulos L, Mlawer E. MODELING: the continual Intercomparison of radiation codes (CIRC) assessing anew the quality of GCM radiation algorithms. Bull Am Meteorol Soc 2010;91(3):305–10.
[40] Oreopoulos L, Mlawer E, Delamere J, Shippert T, Cole J, Fomin B, Rossow WB. The continual intercomparison of radiation codes: results from phase I. J Geophys Res: Atmos 2012;117(D6).

Please cite this article as: Taylor M, et al. Neural network radiative transfer solvers for the generation of high resolution solar irradiance spectra parameterized by cloud and aerosol parameters. J Quant Spectrosc Radiat Transfer (2015), http://dx.doi.org/10.1016/j.jqsrt.2015.08.018

[41] Pearson K. Notes on regression and inheritance in the case of two parents. Proc R Soc Lond 1895;58:240–2 June 20.
[42] Pinker RT, Laszlo I, Tarpley JD, Mitchel K. Geostationary satellite parameters for surface energy balance. Adv Sp Res 2002;30(11): 2427–32.
[43] Pinker RT, et al. Surface radiation budgets in support of the GEWEX Continental-Scale International Project (GCIP) and the GEWEX Americas Prediction Project (GAPP), including the North American Land Data Assimilation System (NLDAS) Project. J Geophys Res 2003;108(D22):8844. http://dx.doi.org/10.1029/2002JD003301.
[44] Park SC, Park MK, Kang MG. Super-resolution image reconstruction: a technical overview. IEEE Signal Process Mag 2003;20:21–36.
[45] Pierluissi JH, Maragoudakis CE. Molecular transmission band models for LOWTRAN. AFGL-TR-86-0272, AD A180655; 1986.
[46] Ricchiazzi P, Yang S, Gautier C, Sowle D. SBDART: A research and teaching software tool for plane-parallel radiative transfer in the Earth's atmosphere. Bull Am Meteorol Soc 1998;79:2101–14.
[47] Rumelhart DE, Hinton GE, Williams RJ. Learning representations by backpropagating errors. Nature 1986;323:533–6.
[48] Sauer T, Yuan X. On multivariate lagrange interpolation. Math Comput 1995;64:1147–70.
[49] Shapiro A, Schmutz W, Thuillier G, Schoell M, Haberreiter M, Rozanov E. Modeling of the current TSI and SSI and its reconstruction to the Past. In: Proceedings of 38th COSPAR scientific assembly, vol. 134; 2010.
[50] Shettle EP. Models of aerosols, clouds and precipitation for atmospheric propagation studies. In: Proceedings of AGARD conference 454 on atmospheric propagation in the UV, visible, IR and MM-region and related system aspects; 1989.
[51] Stamnes K, Tsay S, Wiscombe W, Jayaweera K. Numerically stable algorithm for discrete-ordinatemethod radiative transfer in multiple scattering and emitting layered media. Appl Opt 1988;27:2502–9.
[52] Schwartz SE, Charlson RJ, Kahn R, Rodhe H. Earth's climate sensitivity: apparent inconsistencies in recent assessments. Earth's Future 2014.
[53] Szilder K, Lozowski EP, Reuter GW. A stochastic model of global atmospheric response to enhanced greenhouse warming with cloud feedback. Atmos Res 1998;47–48:475–89.
[54] Takenaka H, Nakajima TY, et al. Estimation of solar radiation using a neural network based on radiative transfer. J Geophys Res 2011. http://dx.doi.org/10.1029/2009JD013337 D08215.
[55] Taylor M, Kazadzis S, Tsekeri A, Gkikas A, Amiridis V. Satellite retrieval of aerosol microphysical and optical parameters using neural networks: a new methodology applied to the Sahara desert dust peak. Atmos Meas Tech 2014;7:3151–75.
[56] Tsushima Y, Manabe S. Influence of cloud feedback on annual variation of global mean surface temperature. J Geophys Res 2001;106 (D19):22635–46. http://dx.doi.org/10.1029/2000JD000235.
[57] Wang Z, Bovik AC, Sheikh HR, Simoncelli EP. Image quality assessment: from error visibility to structural similarity. IEEE Trans Image Process 2004;13(4):600–12.
[58] Zarzalejo LF, Ramirez L, Polo J. Artificial intelligence techniques applied to hourly global irradiance estimation from satellite derived cloud index. Energy 2005;30:1685–97.
[59] Zhang MH, Hack JJ, Kiehl JT, Cess RD. Diagnostic study of climate feedback processes in atmospheric general circulation models. J Geophys Res 1994;99(D3):5525–37. http://dx.doi.org/10.1029/93JD03523.
[60] Zhang Y, Rossow WB, Lacis AA, Oinas V, Mishchenko MI. Calculation of radiative fluxes from the surface to top of atmosphere based on ISCCP and other global data sets: refinements of the radiative transfer model and the input data. J Geophys Res 2004;109: D19105. http://dx.doi.org/10.1029/ 2003JD004457.
[61] Zhong W, Haigh JD. An efficient and accurate correlated-*k* parameterization of infrared radiative transfer for troposphere–stratosphere–mesosphere GCMs. Atmos Sci Lett 2001. http://dx.doi.org/10.1006/asle.2000.0022.

Please cite this article as: Taylor M, et al. Neural network radiative transfer solvers for the generation of high resolution solar irradiance spectra parameterized by cloud and aerosol parameters. J Quant Spectrosc Radiat Transfer (2015), http://dx.doi.org/10.1016/j.jqsrt.2015.08.018